Available online at www.sciencedirect.com

jmr&t Journal of Materials Research and Technology

journal homepage: www.elsevier.com/locate/jmrt

Original Article

Scratch, fretting, and sliding wear of a ZrB_2–hardened Zr_3Al_2 intermetallic–ceramic composite

Jesús López-Arenal [a], *Bibi Malmal Moshtaghioun* [a,*], *Diego Gómez-García* [a], *Angel L. Ortiz* [b,**]

[a] *Departamento de Física de la Materia Condensada, Universidad de Sevilla, Sevilla, 41080, Spain*
[b] *Departamento de Ingeniería Mecánica, Energética y de los Materiales, Universidad de Extremadura, Badajoz, 06006, Spain*

ARTICLE INFO

Article history:
Received 20 December 2022
Accepted 8 February 2023
Available online 11 February 2023

Keywords:
Intermetallic–ceramic composites
Zr–Al intermetallic
Scratch wear
Fretting wear
Sliding wear

ABSTRACT

The unlubricated wear behaviour of a very recently developed ZrB_2–hardened Zr_3Al_2 intermetallic–ceramic composite was investigated for the first time. In particular, tribological tests of scratch, fretting, and sliding were performed with no external lubrication under varied loads against diamond counterparts to thus account for different types and conditions of frictional contacts, and the worn surfaces were characterised in detail to identify the corresponding wear modes and mechanisms. It was found that under scratch wear the Zr_3Al_2–ZrB_2 composite undergoes a ductile-to-brittle transition with increasing applied load, with an increasing plastic damage from low loads and eventually also with macro-chipping at intermediate loads and massive meso-/macro-chipping at high loads. It was also found that the Zr_3Al_2–ZrB_2 composite is resistant to both fretting wear and sliding wear, exhibiting low specific wear rates. Thus, under fretting wear it underwent mild damage first by fretting fatigue in the form of slight surface abrasion and then by fretting oxidation with formation of a self-lubricating oxide tribolayer. The severities of the fretting fatigue and fretting oxidation increased with increasing applied load, with the former dominating over the latter for low and intermediate loads and the opposite being the case for high loads. Similarly, under sliding wear it also underwent only mild damage, now first by mechanical sliding wear and then by oxidative sliding wear, both of increasing severity with increasing applied load, but with the abrasion dominating over the oxidation. Given the promising wear behaviour observed in this first tribological study against diamond, it is proposed that these Zr_3Al_2–ZrB_2 composites merit further investigation under an ample set of possible engineeringly-relevant wear conditions.

* Corresponding author.
** Corresponding author.
E-mail addresses: mali_moshtagh@us.es (B.M. Moshtaghioun), alortiz@unex.es (A.L. Ortiz).

https://doi.org/10.1016/j.jmrt.2023.02.049

1. Introduction

Monolithic intermetallics and intermetallic matrix composites are widely used in a myriad of structural applications because they offer an adequate balance between the desirable mechanical properties of the metals and ceramics, while remaining, in general, easily processable. This is the case of the Zr–Al intermetallics and composites based on them which, with their interesting combination of physico-chemical properties, are promising candidate materials for structural applications in fields as diverse as the aerospace, automotive, medical, and nuclear [1–8], to name but a few, but whose potential has nonetheless been limited in practice by two main drawbacks. One is that their fabrication by foundry metallurgy is difficult to control because there are 10 intermetallic compounds in the binary Zr–Al system [9], and the other is the low hardness and/or toughness of many of them – for example, Zr_5Al_4, Zr_3Al_2, Zr_5Al_3, Zr_2Al, and Zr_3Al are relatively soft (*i.e.*, ~4.5, 5.6, 4.7, 7, and 8 GPa, respectively), and $ZrAl_3$, $ZrAl_2$, Zr_2Al_3, ZrAl, Zr_4Al_3, and Zr_3Al are classifiable as brittle [1]. As a possible solution, it has recently been shown [10] that it is feasible to fabricate composites based on Zr–Al intermetallics with ceramic second phases in a controlled and simple way by powder metallurgy, in particular by means of high-energy ball-milling and reactive spark-plasma sintering (SPS), a proof-of-concept validated by way of example on ZrB_2–hardened Zr_3Al_2 because the Zr_3Al_2 intermetallic is soft but ductile [10]. This novel composite has a hardness of ~11.5 GPa, which is twice that of the Zr_3Al_2 intermetallic, and a fracture toughness of ~4.5 MPa $m^{1/2}$, which is comparatively greater than that of many typical structural ceramics. Therefore, these novel Zr_3Al_2–ZrB_2 composites, and many others fabricated similarly based on other Zr–Al intermetallics with ZrB_2 or other ceramic second phases, could become appealing structural materials.

The development of the ZrB_2–hardened Zr_3Al_2 composites is currently still in such an early phase that the only information available on their mechanical properties is hardness and fracture toughness [10]. This is clearly insufficient if these materials are to be put into service in structural applications, for which reason it is crucially important to generate much

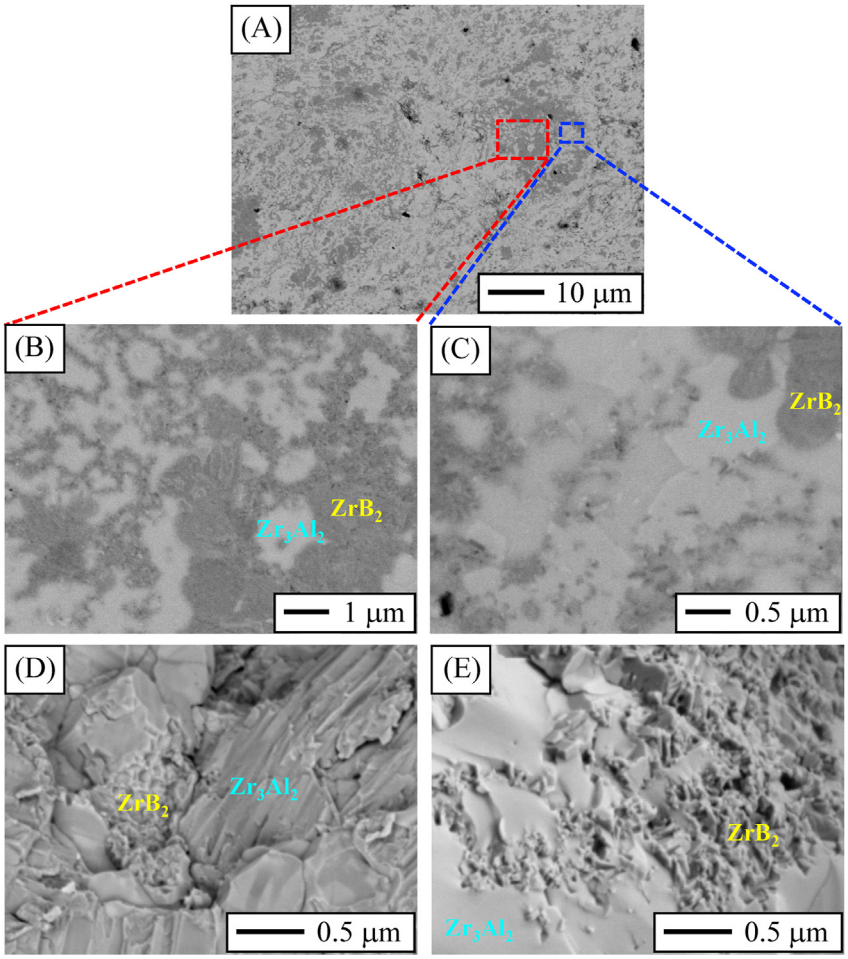

Fig. 1 – FE-SEM images of the microstructure of the material fabricated by SPS at 1200 °C/50 MPa/5 min from the as-milled $2ZrH_2$:1Al:1B powder mixture. (A) Low-magnification FE-SEM image taken on the polished surface and (B)–(C) higher-magnification FE-SEM images of the regions marked in (A). (D)–(E) High-magnification FE-SEM images taken on the fracture surface in regions of the microstructure rich in Zr_3Al_2 intermetallic and in ZrB_2 ceramic, respectively. FE-SEM imaging was done with backscattered electrons.

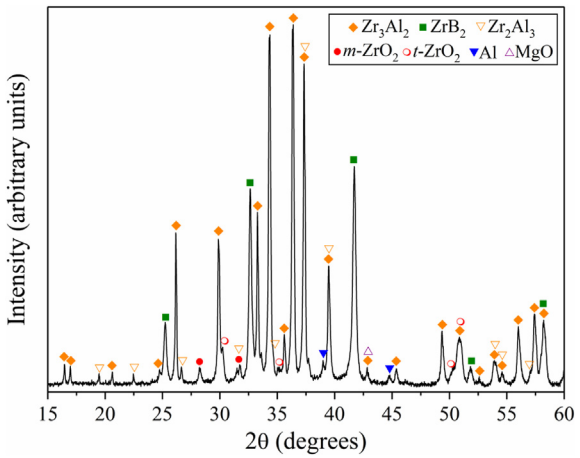

Fig. 2 – XRD pattern (15–60° 2θ) of the material fabricated by SPS at 1200 °C/50 MPa/5 min from the as-milled $2ZrH_2$:1Al:1B powder mixture. Peak assignations are included. The XRD pattern was acquired with CuKα incident radiation and was indexed using the PDF2 database. The letters *m* and *t* mean monoclinic and tetragonal, respectively.

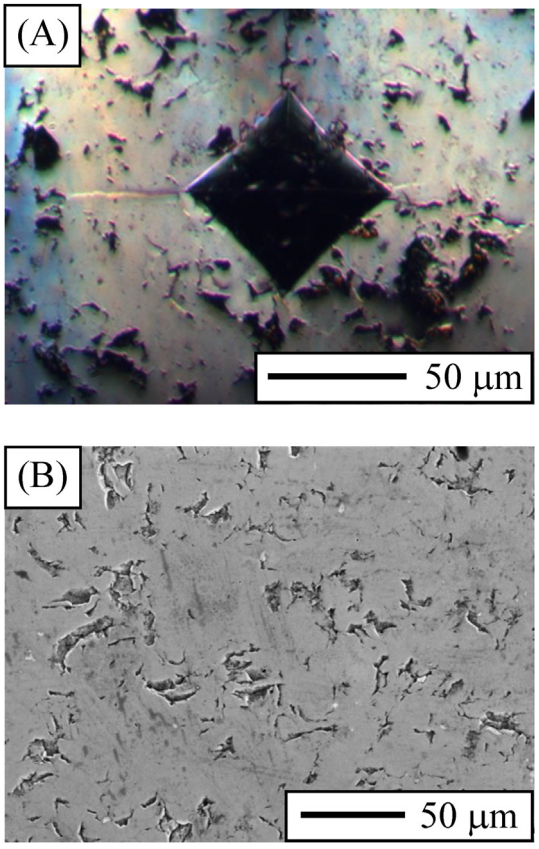

Fig. 3 – (A) Bright-field OM image of a residual indent made on the ZrB_2–hardened Zr_3Al_2 intermetallic–ceramic composite at 29.4 N load, and (B) an SEM image of its surface after grinding and polishing. Pitted zones are not pores, but micro-chips generated during the grinding and polishing stages.

more knowledge in this area. For example, one attribute that deserves immediate study is their wear behaviour, defined as the susceptibility to surface and sub-surface damage due to frictional contacts [11]. Studying their wear is important not only because these intermetallic–ceramic composites could be used as components in a myriad of tribological applications, but also because wear may occur innately in any engineering application and pose a major threat to their structural integrity in service (for example, by lowering their strength).

With these premises in mind, the present study was aimed at investigating, for the first time, the wear behaviour of the recently-developed ZrB_2–hardened Zr_3Al_2 composites. Also, since there is no previous information on the matter, this first model tribological study examines three basic types of wear, namely, scratch (*i.e.*, unidirectional motion of an abrasive along a surface), fretting (*i.e.*, short-amplitude reciprocating motion between two surfaces in contact for a large number of cycles), and sliding (*i.e.*, unidirectional motion between two surfaces in contact for a large distance) [11–13] against a much harder counterpart (*i.e.*, diamond) in the absence of external lubrication, paying especial attention to identifying the wear modes and mechanisms.

2. Experimental procedure

The processing of the ZrB_2–hardened Zr_3Al_2 composite followed the procedure described in detail elsewhere [10]. Very briefly, commercially available (MaTecK, Germany) powders of ZrH_2 (99.7% purity), Al (99.8% purity), and B (95% purity) were combined in molar ratios $2ZrH_2$:1Al:1B, and subjected to high-energy ball-milling for 30 min in a shaker mill (Spex D8000, Spex CertiPrep, USA) under Ar atmosphere. The as-milled powder mixture was then loaded into graphite dies lined with graphite foils and covered by graphite blankets, and densified by SPS (HP-D-10, FCT Systeme GmbH, Germany) in dynamic vacuum at 1200 °C (as measured by an axial pyrometer and reached at 100 °C/min) for 5 min under 50 MPa pressure (applied at 300 °C). The resulting ZrB_2–hardened Zr_3Al_2 intermetallic composite was ground and diamond-polished to a 0.25-μm finish, and was characterised (i) microstructurally by field-emission scanning electron microscopy (FE-SEM; FEI Teneo, FEI Inc., USA) together with energy-dispersive X-ray spectroscopy (EDS; Ametek, Inc., USA) and X-ray diffractometry (XRD; D8 Advance, Bruker AXS, Germany), as well as (ii) mechanically (*i.e.*, hardness and fracture toughness) by Vickers indentation tests (Duramin, Struers A/S, Denmark).

Importantly, given the context of the present study, the ZrB_2–hardened Zr_3Al_2 composite was also characterised tribologically by unlubricated wear tests under different geometries and conditions of frictional contact, under ambient conditions, as will be described in what follows. First, scratch-wear tests were performed (Revetest RST3, Anton Paar, Austria) using a 200-μm radius Rockwell-C diamond tip, under both progressive and constant loads. The former were carried out with linearly-increasing loads in the range 1–100 N, at 10 N/min load rate, 0.3 mm/min scratch speed, and 3 mm scratch distance, and the latter were carried out at 5, 15, 40,

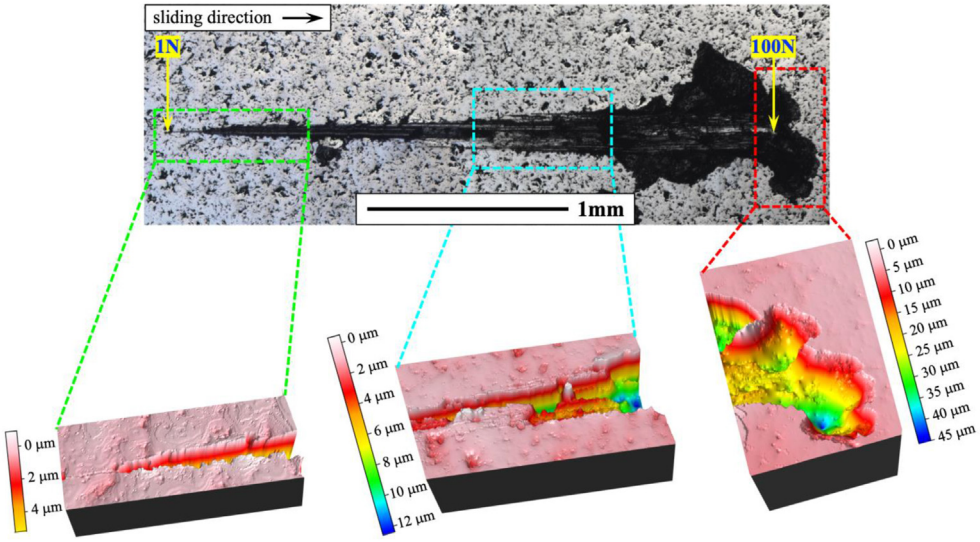

Fig. 4 – Bright-field OM image (panoramic view) of the residual scratch track generated in the present ZrB_2–hardened Zr_3Al_2 intermetallic–ceramic composite during the test at progressive loads between 1 and 100 N, as well as 3-D OP images of the three regions of the scratch track marked in the OM image. The sliding direction is indicated. Pitted zones are not pores, but micro-chips generated during the grinding and polishing stages.

and 80 N loads, 0.3 mm/min scratch speed, and 3 mm scratch distance. Second, fretting-wear tests were performed (MFT-3000, Rtec Instruments, USA) at 2, 8, 15, 30, and 50 N loads, 10 Hz frequency, 55 μm stroke, and a duration of 100 000 back-and-forth cycles, using diamond-coated SiC balls (Dball G10, Nova Diamant, UK) as counterparts. And third, sliding-wear tests were performed (MFT-3000, Rtec Instruments, USA) in the ball-on-disk configuration at 20 and 40 N loads, 10 cm/s linear sliding speed, 2 mm track radius, and 1000 m total sliding distance, using diamond-coated SiC balls (Dball G10, Nova Diamant, UK) as counterparts. The use of a diamond tip and diamond-coated balls as counterparts was to simulate the scenario of wear against the hardest material known by man. The worn surfaces of the ZrB_2–hardened Zr_3Al_2 composite were examined by optical microscopy (OM; Epiphot 300, Nikon, Japan), optical profilometry (OP; Profilm 3D, Filmetric, USA), and scanning electron microscopy (SEM; S-3600 N, Hitachi, Japan) together with EDS (flash Detector 3001, Röntec GmbH, Germany) as needed to inspect the wear-induced damage at both the macroscopic and microscopic scales. The contact surfaces of the counter-balls were also examined by OM.

3. Results and discussion

3.1. *Microstructure and hardness–toughness*

Fig. 1 shows FE-SEM images of the microstructure of the material resulting from the reactive SPS at 1200 °C/50 MPa/5 min of the as-milled $2ZrH_2$:1Al:1B powder mixture. It can be seen in the low-magnification FE-SEM image shown in Fig. 1A, taken on the polished surface, that the material is fully dense, a fact that direct density measurements by the Archimedes method confirmed (*i.e.*, absolute density of ~5.452(6) g/cm^3, which is essentially the expected theoretical density). It is also evident in Fig. 1A, and even more so in the higher-magnification FE-SEM images of Fig. 1B and C, that, as expected from the reaction stoichiometry (*i.e.*, $4ZrH_2+2Al+2B \rightarrow 4Zr+2Al+2B+4H_2(g) \rightarrow Zr_3Al_2+ZrB_2$), this material is indeed an intermetallic–ceramic composite with an essentially bi-phasic microstructure, with the lighter phase identified by EDS as Zr_3Al_2 intermetallic and

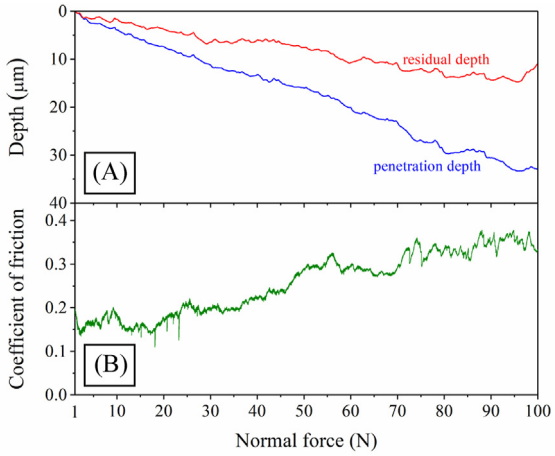

Fig. 5 – (A) Curves of penetration depth and residual depth as functions of the applied load corresponding to the scratch test at progressive load (1–100 N) performed on the present ZrB_2–hardened Zr_3Al_2 intermetallic–ceramic composite. The former was logged during the scratch test itself, and the latter by a post-scan with the diamond tip along the scratch track at 0.5 N. Both curves were corrected by the surface profile logged by a pre-scan with the diamond tip at 0.5 N load. (B) Curve of friction (*i.e.*, CoF as a function of the applied load) logged during the scratch test at progressive load (1–100 N).

the darker phase as ZrB_2 ceramic. Also, the microstructure seems very fine, apparently with grain sizes below the micrometre scale. Certainly, the high-magnification FE-SEM images shown in Fig. 1D and E, taken on the fracture surface, reveal that the Zr_3Al_2 grains are submicrometre or nearly submicrometre, and that what seemed to be coarse ZrB_2 grains in Fig. 1B and C are actually clusters of ZrB_2 nanograins (of ~50–60 nm in average size).

Fig. 2 shows the XRD pattern of this material, confirming the deduction already made from FE-SEM/EDS that it is, essentially, a bi-phasic composite constituted by Zr_3Al_2 and ZrB_2. It is true that there are other phases, but these are very minor or even almost negligible. Indeed, the very little ZrO_2 is attributable to a slight spontaneous passivation of ZrH_2 prior to SPS, the traces of MgO to Mg being a typical impurity in B powders, and the very little Al and Zr_2Al_3 to the formation of ZrO_2 having left less Zr available to form Zr_3Al_2 thus giving rise to unreacted Al or to an Al-richer Zr–Al intermetallic.

Regarding the mechanical properties, the Vickers indentation tests determined that the present Zr_3Al_2–ZrB_2 composite possesses (i) a hardness of ~11.5 GPa, which is twice that expected for Zr_3Al_2 monolithic intermetallics (*i.e.*, ~5.5 GPa), and (ii) a moderate fracture toughness of ~4.5 $MPa \cdot m^{1/2}$. Therefore, this ZrB_2–hardened Zr_3Al_2 intermetallic–ceramic composite has hardness and toughness intermediate between those of metals and ceramics, being harder but more brittle than the former and softer but tougher than the latter. Interestingly, during the observation of the Vickers indents by OM, such as the micrograph shown by way of example in Fig. 3A, it was noted that this Zr_3Al_2–ZrB_2 composite had undergone, due to its bi-phasic nature (*i.e.*, weak interfaces deriving from the residual thermo-elastic stresses [14,15]), pervasive but shallow micro-chipping [16] during the grinding and polishing stages, an example of which is shown in the SEM image of Fig. 3B.

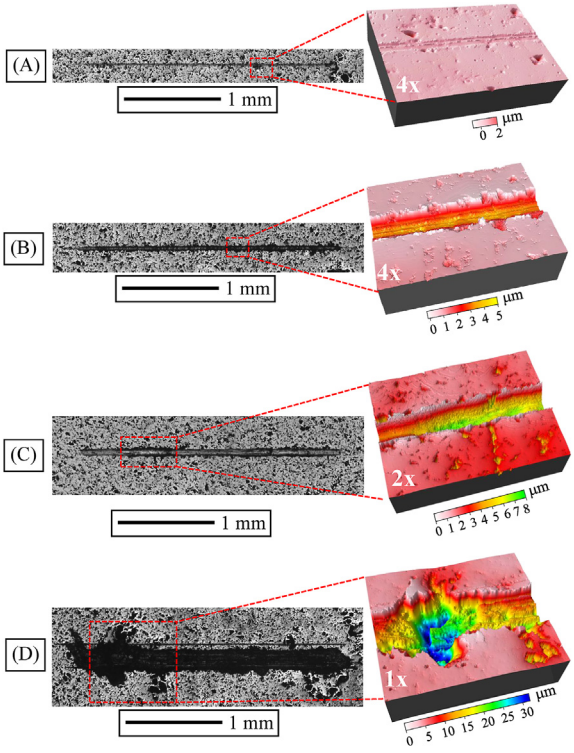

Fig. 6 – Bright-field OM images (panoramic views) of residual scratch tracks generated in the ZrB_2–hardened Zr_3Al_2 intermetallic–ceramic composite during the tests at constant loads of (A) 5, (B) 15, (C) 40, and (D) 80 N, as well as a 3-D OP image of the region of each of them marked in the OM image. Pitted zones are not pores, but micro-chips generated during the grinding and polishing stages. The numbers 4×, 2×, and 1× in the 3-D OP images denote the degree of relative magnification between them.

3.2. *Scratch wear*

Fig. 4 shows an OM image (panoramic view) of the residual scratch track produced in the ZrB_2–hardened Zr_3Al_2 intermetallic–ceramic composite during the test at linearly-increasing progressive loads in the range 1–100 N, as well as detailed 3-D OP images of three zones of that track (*i.e.*, regions of low, medium, and high scratch loads). It can be seen that, as expected from increasing severity of the sliding contact, the width and depth of the scratch track increase with increasing applied load. More importantly, it can also be seen that the damage pattern evolves from initial plasticity-induced surface smoothing at low loads to severe fracture-induced chipping at high loads [16–18]. The curves of penetration depth–applied load and residual depth–applied load shown in Fig. 5 (Fig. 5A) confirm the increasing scratch track as load increases, and, which is more important, their comparison also indicates that (i) due to its ZrB_2 ceramic phase, the Zr_3Al_2–ZrB_2 composite has a good capacity for elastic recovery, and (ii) due to its Zr_3Al_2 intermetallic phase, the Zr_3Al_2–ZrB_2 composite did not fracture within the elastic deformation regime but after a certain plastic deformation. Finally, as can also be seen in Fig. 5 (Fig. 5B), the load increase came accompanied by a greater coefficient of friction (CoF), indicative of increasingly rough contact.

Fig. 6 shows OM images (panoramic views) of the scratch tracks produced in the ZrB_2–hardened Zr_3Al_2

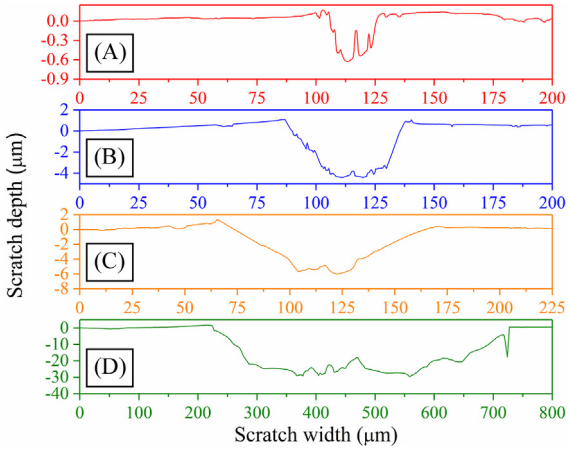

Fig. 7 – Typical 2-D OP profiles of the residual scratch tracks generated in the ZrB_2–hardened Zr_3Al_2 intermetallic–ceramic composite during the tests at constant loads of (A) 5, (B) 15, (C) 40, and (D) 80 N, as extracted from corresponding 3-D OP images in Fig. 6.

intermetallic–ceramic composite during the tests at selected constant loads of 5, 15, 40, and 80 N, as well as 3-D OP images of a zone of each of them, and Fig. 7 a set of 2-D OP profiles extracted from the 3-D OP images. These additional observations and analyses confirm the change of damage pattern observed in the progressive-load scratch tests. Indeed, it can be seen that at 5 N load (Figs. 6A-7A) the scratch track is very narrow and shallow (*i.e.*, ~25 μm and 0.6 μm), indicative of a very superficial scar. At 15 N load (Figs. 6B-7B), the scratch track is wider and deeper (*i.e.*, ~50 μm and 4 μm), but still relatively superficial, and there is already evidence of incipient ridges and minor chipping along the scratch track contour. At 40 N load (Figs. 6C-7C), the scratch track is even wider and deeper (*i.e.*, ~100 μm and 6 μm) and has better-defined ridges on both sides, and chipping is more copious. And finally, at 80 N load (Figs. 6D-7D), the scratch track is extremely wide and deep (*i.e.*, ~500 μm and 30 μm), and there is massive chipping as well as other areas about to chip.

Fig. 8 shows SEM images of the scratch damage generated in the ZrB_2–hardened Zr_3Al_2 intermetallic–ceramic composite at different loads. It can be seen that at 5 N load (Fig. 8A) there is very little damage, and that this is in the form of grooves parallel to the scratch direction and subtle ridges both caused by ploughing (*i.e.*, by plastic deformation) [11]. At 15 N load (Fig. 8B) there is more of such plastic damage, indicative of more severe ploughing, plus fracture-induced macro-chipping [16] but limited to the near contour of the scratch track. The scenario at 40 N load (Fig. 8C) is qualitatively similar, but quantitatively with more plastic damage inside the scratch track and more copious macro-chipping. And finally, at 80 N load (Fig. 8D) the damage is very severe, and in the form of considerable plastic deformation and macro-chipping inside the scratch track (Fig. 8E) as well as profuse meso-chipping outside the scratch track (Fig. 8F). Interestingly, no evidence was observed of radial cracks outside the scratch track, nor of the more detrimental cone cracks in its interior that are typically associated with great brittleness [19].

Taken together, this set of observations and results indicates that, under scratching, the present ZrB_2–hardened Zr_3Al_2 intermetallic–ceramic composite undergoes a ductile-to-brittle transition with increasing load, where the initial plastic damage would be shear-driven plasticity (*i.e.*, discrete shear faults, dislocations, twins, *etc.*) and the eventual macro- and meso-chipping would be the result of the propagation and intersection with a free surface of sub-surface lateral cracks initiated in plastic deformation zones and would occur to

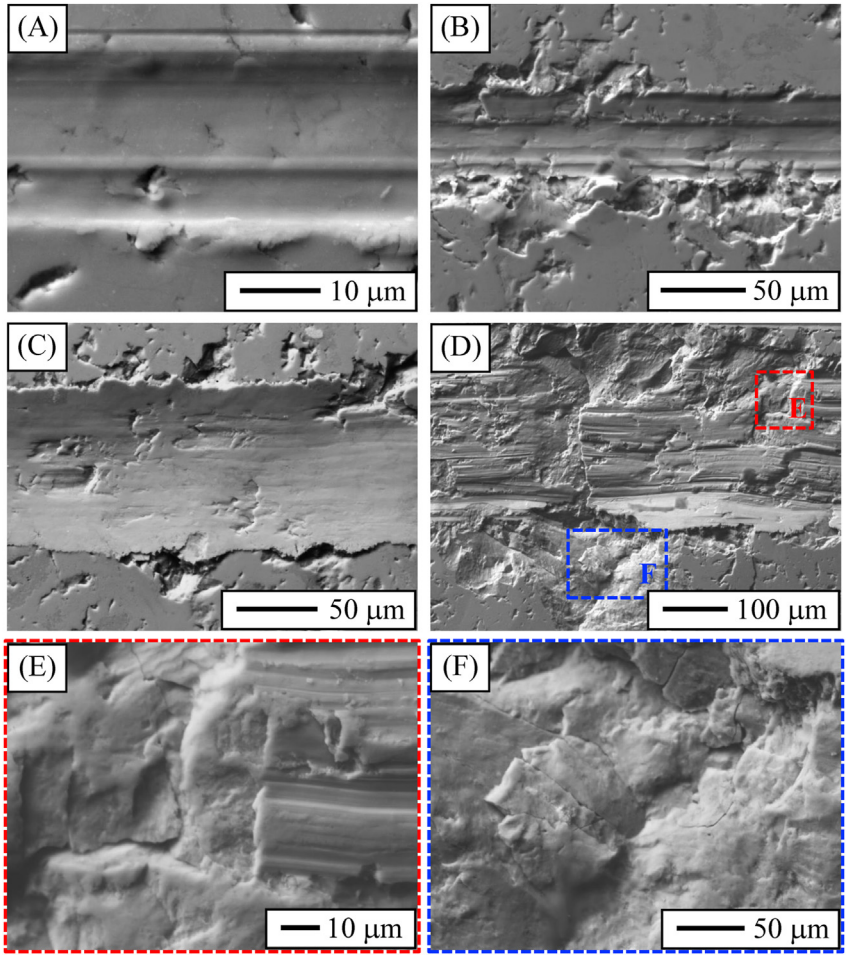

Fig. 8 – SEM images of the damage inside and outside the residual scratch tracks generated in the ZrB_2–hardened Zr_3Al_2 intermetallic–ceramic composite during the tests at constant loads of (A) 5, (B) 15, (C) 40, and (D) 80 N, as well as (E)–(F) higher-magnification SEM images of the regions marked in (D).

relax the nearby residual stress field [16]. Plastic damage, while being less harmful than brittle damage, is thus not benign in terms of mechanical integrity. More specifically, there is a first ductile regime at the lowest loads exclusively with plasticity, in which the mild plastic deformation results only in smooth surface "polishing". This is followed by a second "quasi-brittle" regime at intermediate loads already with plasticity and fracture, in which the greater plastic damage results in an increasing yield zone with the attendant extrusion of material at the contour of the scratch track while also causing moderate fracture-driven macro-chipping. And finally there is a last brittle regime at the highest loads, in which the severe plastic damage comes accompanied by internal macro-chipping and massive external meso-chipping.

3.3. *Fretting wear*

Fig. 9 shows the friction curves logged during the fretting tests performed on the ZrB_2–hardened Zr_3Al_2 intermetallic–ceramic composite at selected loads in the range 2–50 N. It can be seen that the friction is very low in all cases, with steady-stage CoFs as strikingly low as only 0.03–0.04 that indicate very little resistance to the oscillatory relative motion. This rules out the occurrence of partial slip [20] while suggesting that the Zr_3Al_2–ZrB_2 composite would have undergone only mild fretting wear. Indeed, these low CoFs are typical of lubricated contacts [11], thus indicating that there was a self-lubrication mechanism operative during the fretting tests because these were carried out under unlubricated conditions (*i.e.*, with no external lubricant). It can also be seen in Fig. 9 that, while the steady-state CoFs were eventually nearly the same, the run-in stage lasted significantly longer for the fretting test at 2 N load (*i.e.*, ~30 000 cycles) than for the other fretting tests at higher loads (*i.e.*, ~1 000 cycles), thus indicating delayed self-lubrication in the former.

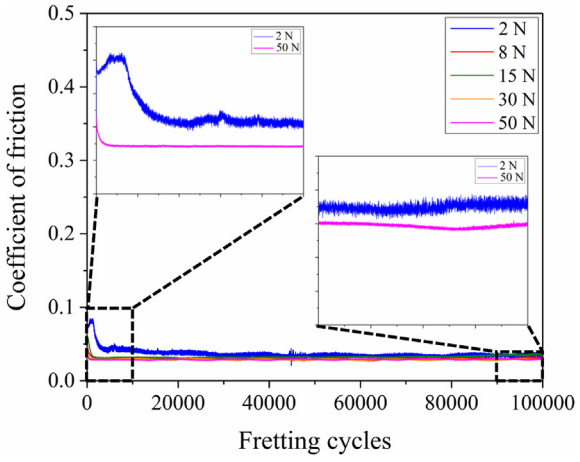

Fig. 9 – Curves of friction (*i.e.*, CoF as a function of the fretting cycles) logged during the fretting tests performed on the ZrB_2–hardened Zr_3Al_2 intermetallic–ceramic composite at loads in the range 2–50 N. The insets within the figure compare in more detail the friction curves corresponding to the fretting tests at extreme loads of 2 and 50 N during the first and last 10 000 cycles.

Fig. 10 shows OM images of the residual fretting tracks produced in the ZrB_2–hardened Zr_3Al_2 intermetallic–ceramic composite during the tests at loads of 2–50 N, as well as complete 3-D OP images of those tracks. It can be seen in the OM images that the size of the fretting tracks increases with increasing applied load – *i.e.*, lengths and widths of ~160 μm and 115 μm at 2 N load (Fig. 10A), ~180 and 140 μm at 8 N load (Fig. 10B), ~205 μm and 150 μm at 15 N load (Fig. 10C), ~215 μm and 180 μm at 30 N load (Fig. 10D), and ~230 μm and 200 μm at 50 N load (Fig. 10E) – thus indicating the occurrence of greater damage, and also that in all cases the length of the fretted zone is between 3 and 4 times greater than the nominal stroke of 55 μm imposed as condition during the fretting tests. This is due to the deformation, probably initially elastic, of the contact, which is logically greater with increasing applied load. Interestingly, the fact that the length of the fretting tracks is less than twice their width indicates the occurrence, as expected, of gross slip [20], which is the fretting regime in which the entire contact has slipped during the reciprocating cycle but not so much as to reach the regime of reciprocating sliding (*i.e.*, length greater than twice the width) [20].

Importantly, the 3-D OP images also shown in Fig. 10 demonstrate that, while the fretting damage increases with increasing applied load, it is very superficial, thus confirming the occurrence of only mild fretting as was already anticipated from the low CoFs in Fig. 9. Indeed, the fretting track generated at 2 N load is almost imperceptible under OP (Fig. 10A), that generated at 8 N load is just barely discernible (Fig. 10B), while those generated at 15, 30, and 50 N loads are already more noticeable (Fig. 10C–E). Interestingly, as can be seen in Fig. 11, the 2-D OP profiles extracted from these 3-D OP images indicate that the residual fretting tracks generated at 2, 8, and 15 N loads are shallow hollows, while those generated at 30 and 50 N loads are small mounds. This morphological difference does not necessarily imply that the fretting mechanisms are different, but their relative severities do. Excluding the already existing chipping before the fretting tests (Fig. 3B), the volume of the fretted zones at 15 and 50 N loads (the former chosen because it resulted in the deepest hollow, and the latter because it resulted in the highest mound) are estimated to be ~$2.15 \cdot 10^{-6}$ and $8.05 \cdot 10^{-6}$ mm^3, respectively, from which the corresponding specific fretting-wear rates (SFWRs) are calculated to be ~$1.30 \cdot 10^{-8}$ and $1.46 \cdot 10^{-8}$ $mm^3/(N \cdot m)$ or, alternatively, ~$1.43 \cdot 10^{-12}$ and $1.61 \cdot 10^{-12}$ $mm^3/(N \cdot cycle)$, respectively. Importantly, these low SFWRs of the order of 10^{-8} $mm^3/(N \cdot m)$ would class the fretting wear as being very mild [11,12].

Also interestingly, it can be seen in Fig. 10 that apparently, regardless of whether they are hollows or mounds, all the fretted zones exhibit a tribolayer. In principle this could be either carbon (*i.e.*, diamond, or graphite if the diamond has graphitized) transferred from the counter-balls, which is very unlikely given their ultra-high hardness (*i.e.*, >80 GPa), or oxide resulting from the surface oxidation of the contact zone as a consequence of the frictional heating generated during the fretting tests in air atmosphere, which is more likely. By way of example, Fig. 12 shows the SEM images of the complete residual fretting tracks produced at 15 N (Figs. 12A) and 50 N (Fig. 12B) loads (chosen for the same reasons as when calculating the SFWRs), together with the

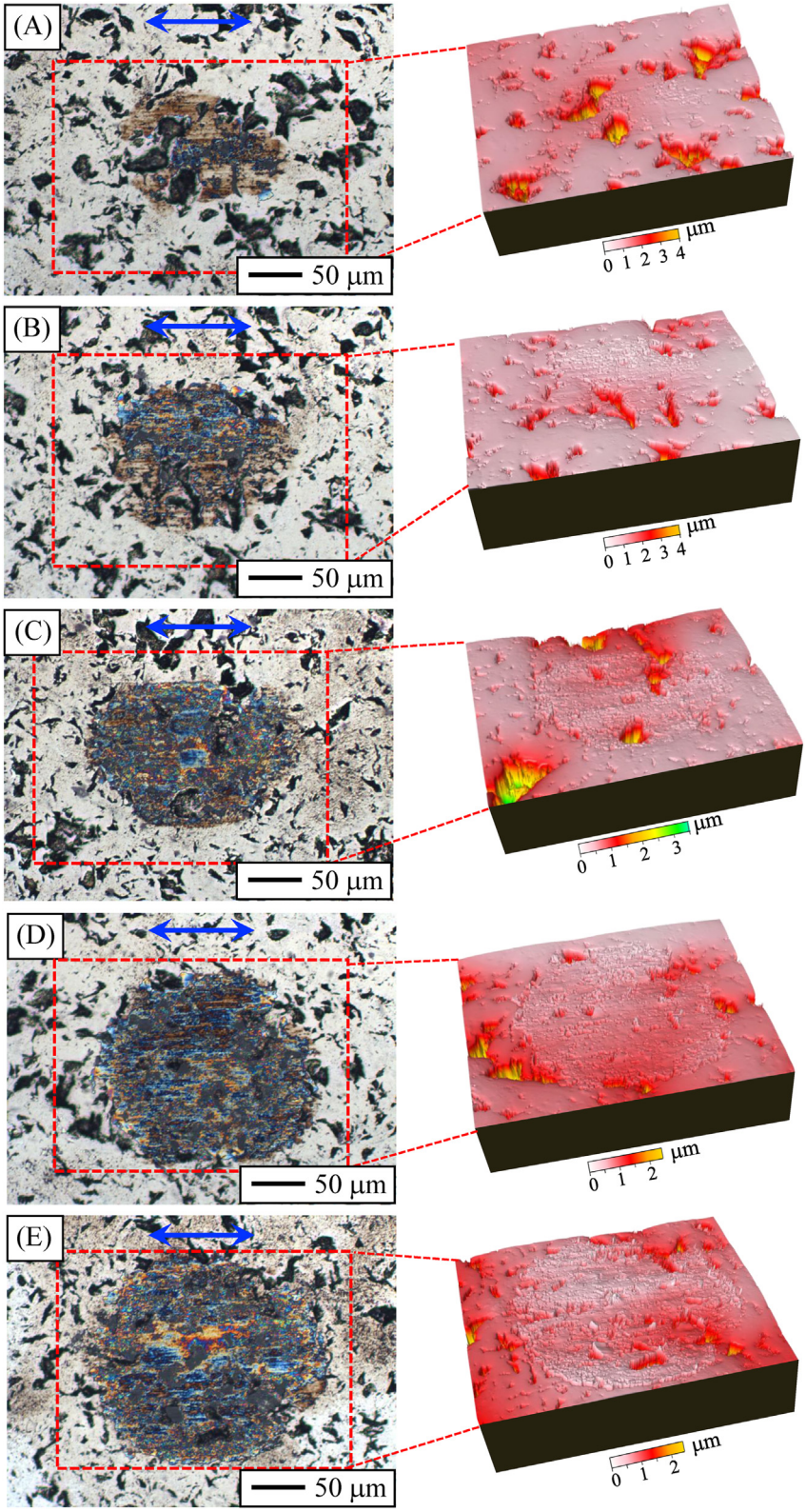

Fig. 10 – Bright-field OM images of the residual fretting tracks generated in the ZrB_2–hardened Zr_3Al_2 intermetallic–ceramic composite during the tests at loads of (A) 2, (B) 8, (C) 15, (D) 30, and (E) 50 N, as well as complete 3-D OP images of them (as marked in the OM images). Pitted zones are not pores, but micro-chips generated during the grinding and polishing stages. The arrows denote the fretting direction.

corresponding elemental composition maps of C and O acquired by EDS to elucidate which of the above two options is the correct one. It is very clear from these composition maps that the tribolayers are, as expected, surface oxide (note that the two carbon maps only show background noise attributable to bremsstrahlung), therefore indicating the occurrence of mild fretting corrosion (and more specifically fretting oxidation). Moreover, examination of the counter-balls by OM, as shown by way of example in Fig. 12C for the fretting test at 30 N load, revealed no damage, thus corroborating that the tribolayers are not carbon. Fig. 13 shows higher-magnification SEM images of the fretting damage generated at the different loads applied. These observations (i) confirm the formation of thin tribolayers (because they are relatively "transparent" to the electron beam) and therefore the occurrence of mild fretting oxidation, and (ii) also show evidence of slight abrasion of the surface underneath, therefore also indicating the occurrence of mild fretting fatigue. It can also be seen that the tribolayers have a smooth (apparently polished) surface, and that they appear well adhered with only some localized partial delamination or spalling. The latter would indicate that the tribolayers must be oxides of both Zr_3Al_2 and ZrB_2 because the Zr_3Al_2 and ZrB_2 rich regions in the bi-phasic microstructure of this composite have micrometre sizes. These oxide tribolayers therefore gave rise to the self-lubrication inferred from the CoFs in Fig. 9 because oxides have a low shear strength [11], and the earlier they formed the earlier self-lubrication started.

Taken together, these observations and results indicate that the present Zr_3Al_2–ZrB_2 composite is resistant to fretting wear – *i.e.*, resistance of the order of 10^7 (N·m)/mm^3, or alternatively of 10^{11} (N·cycle)/mm^3) – and is therefore a potential candidate for the fabrication of components subjected to small oscillatory movements (which nonetheless requires study and validation for each particular tribo-system because other tribo-parts under other fretting conditions may undergo other phenomena such as adhesion, wear debris, *etc.*). In this first study against ultrahard diamond, the Zr_3Al_2–ZrB_2 composite fretted in gross-slip regime, initially undergoing mild fretting fatigue (*i.e.*, slight mechanical abrasion) until an oxide tribolayer eventually formed dictating the onset of mild fretting oxidation. The severities of both the fretting fatigue and the fretting oxidation increased with increasing applied load, but with the former dominating over the latter for loads of 2, 8, and 15 N to give hollow-type fretting tracks, and the contrary being the case with the latter dominating over the former for loads of 30 and 50 N to give mound-type fretting tracks. In any case, once formed, the oxide tribolayers were, because they largely remained in place, "protective" in the sense that (i) they prevented direct contact between the Zr_3Al_2–ZrB_2 composite and the diamond counter-ball, and (ii) they lubricated the contact, thus avoiding much more severe fretting fatigue during the remainder of the fretting tests.

3.4. *Sliding wear*

Fig. 14 shows the friction curves logged during the sliding tests performed on the ZrB_2–hardened Zr_3Al_2 intermetallic–ceramic composite at selected loads of 20 and 40 N. It can be seen that, as in the case of the fretting tests, the friction is also very low, with CoFs lower than 0.1 which (i) indicate very little resistance to the relative sliding presumably due again to the formation of self-lubricating oxide tribolayers, and (ii) suggest

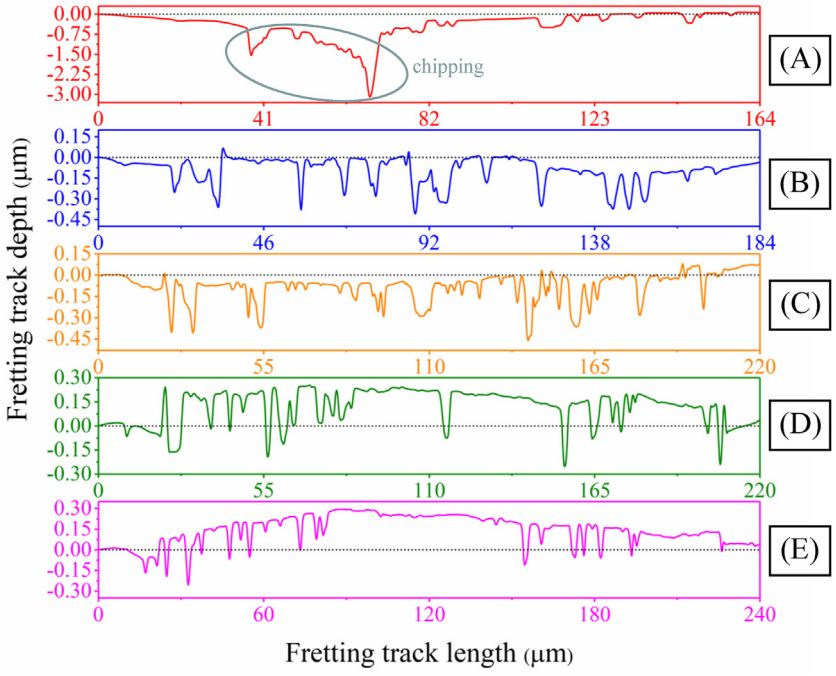

Fig. 11 – Typical 2-D OP profiles of the residual fretting tracks generated in the ZrB_2–hardened Zr_3Al_2 intermetallic–ceramic composite during the tests at loads of (A) 2, (B) 8, (C) 15, (D) 30, and (E) 50 N, as extracted from corresponding 3-D OP images in Fig. 10. The dotted lines denote the zero baseline. The zone marked in (A) is pre-existing chipping, no fretted volume.

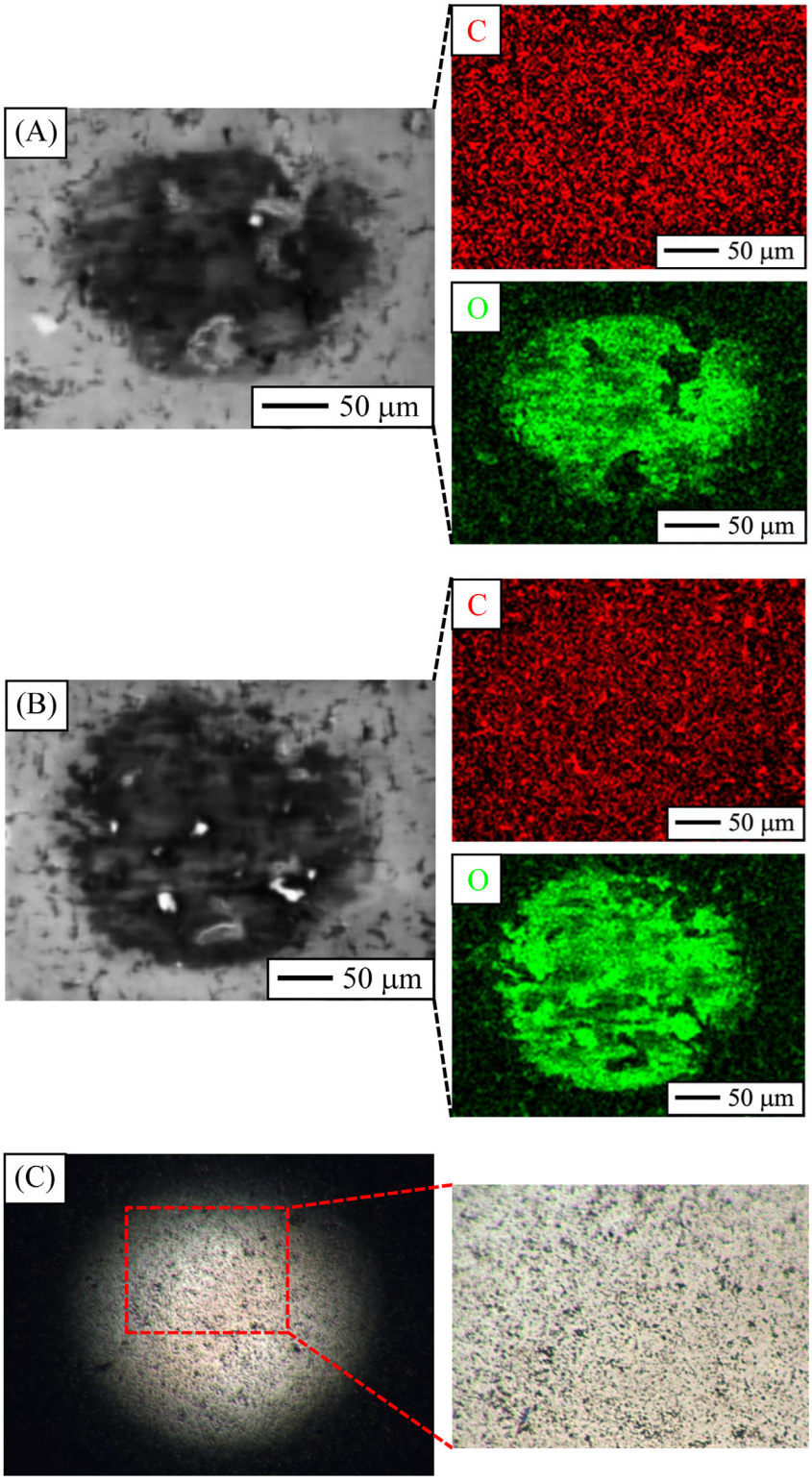

Fig. 12 – Low-magnification SEM images and the corresponding elemental composition maps of C and O acquired by EDS of the complete residual fretting tracks generated in the ZrB_2–hardened Zr_3Al_2 intermetallic–ceramic composite during the tests at loads of (A) 15 and (B) 50 N. Pitted zones are not pores, but micro-chips generated during the grinding and polishing stages. (C) OM image of the counter-ball at the conclusion of the fretting test at 30 N load.

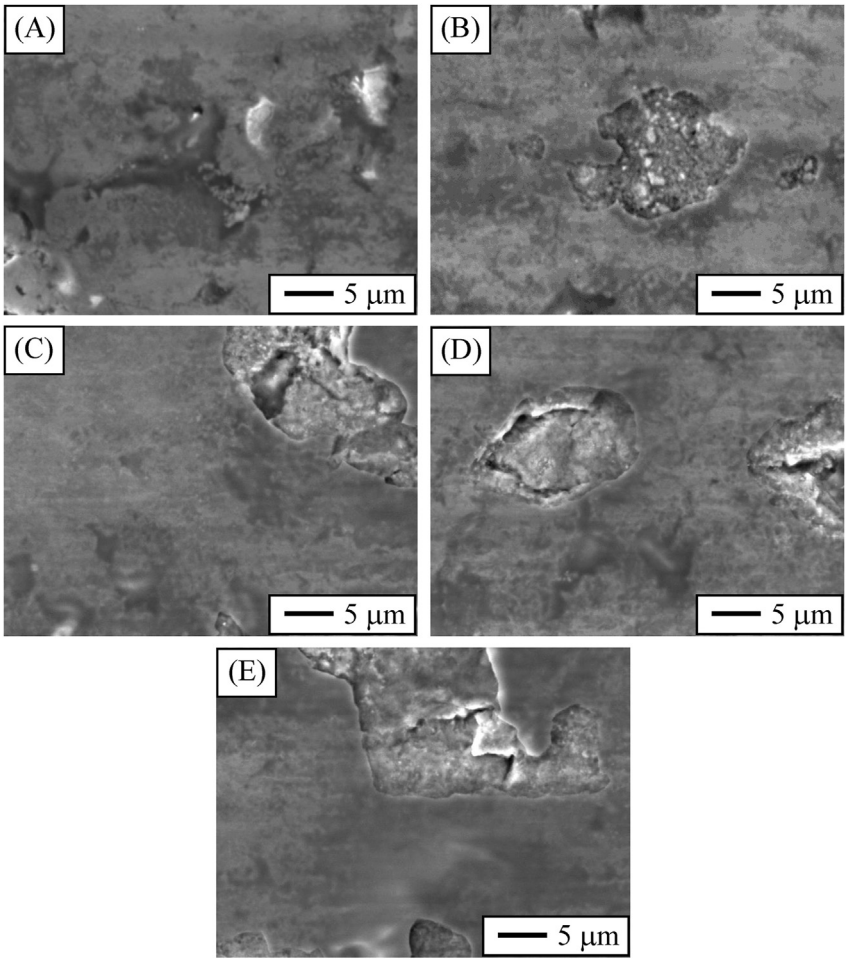

Fig. 13 – SEM images of the damage inside the residual fretting tracks generated in the ZrB_2–hardened Zr_3Al_2 intermetallic–ceramic composite during the tests at loads of (A) 2, (B) 8, (C) 15, (D) 30, and (E) 50 N. Note that these SEM images were intentionally taken at zones where the oxide tribolayers had partially failed, but that lower-magnification SEM images demonstrated that the extent of this phenomenon is limited.

the occurrence of only mild sliding wear. It can also be seen that the friction at 40 N load is slightly less than at 20 N load, which is the same trend with applied load as previously observed for the fretting tests, indicative of more effective self-lubrication.

Fig. 15 shows OM images of the sliding tracks produced in the ZrB_2–hardened Zr_3Al_2 intermetallic–ceramic composite during the tests at 20 and 40 N loads, as well as 3-D OP images of those tracks and 2-D OP profiles in turn extracted from the 3-D OP images. Comparatively, it can be seen in the OM images (Fig. 15A,B–left) that, with increasing applied load, the sliding track is wider, and in the OP images (Fig. 15A,B–right) that it is wider and deeper, thus indicating the occurrence of greater damage. Certainly, the 2-D OP profiles (Fig. 15C) allow to calculate that the width and depth of the sliding tracks are ~190 μm and 0.8 μm at 20 N load, but ~235 μm and 1.6 μm at 40 N load. Note nonetheless that in both cases the sliding track is a shallow hollow, with the corresponding worn volumes being ~$8.13 \cdot 10^{-4}$ and $2.21 \cdot 10^{-3}$ mm^3, respectively. These give specific sliding-wear rates (SSWRs) as low as only ~$4.06 \cdot 10^{-8}$ and $5.54 \cdot 10^{-8}$ $mm^3/(N \cdot m)$, respectively, that would class the

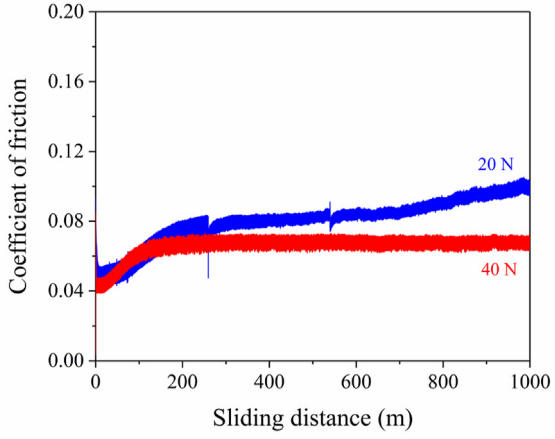

Fig. 14 – Curves of friction (*i.e.*, CoF as a function of the sliding distance) logged during the sliding tests performed on the ZrB_2–hardened Zr_3Al_2 intermetallic–ceramic composite at loads of 20 and 40 N.

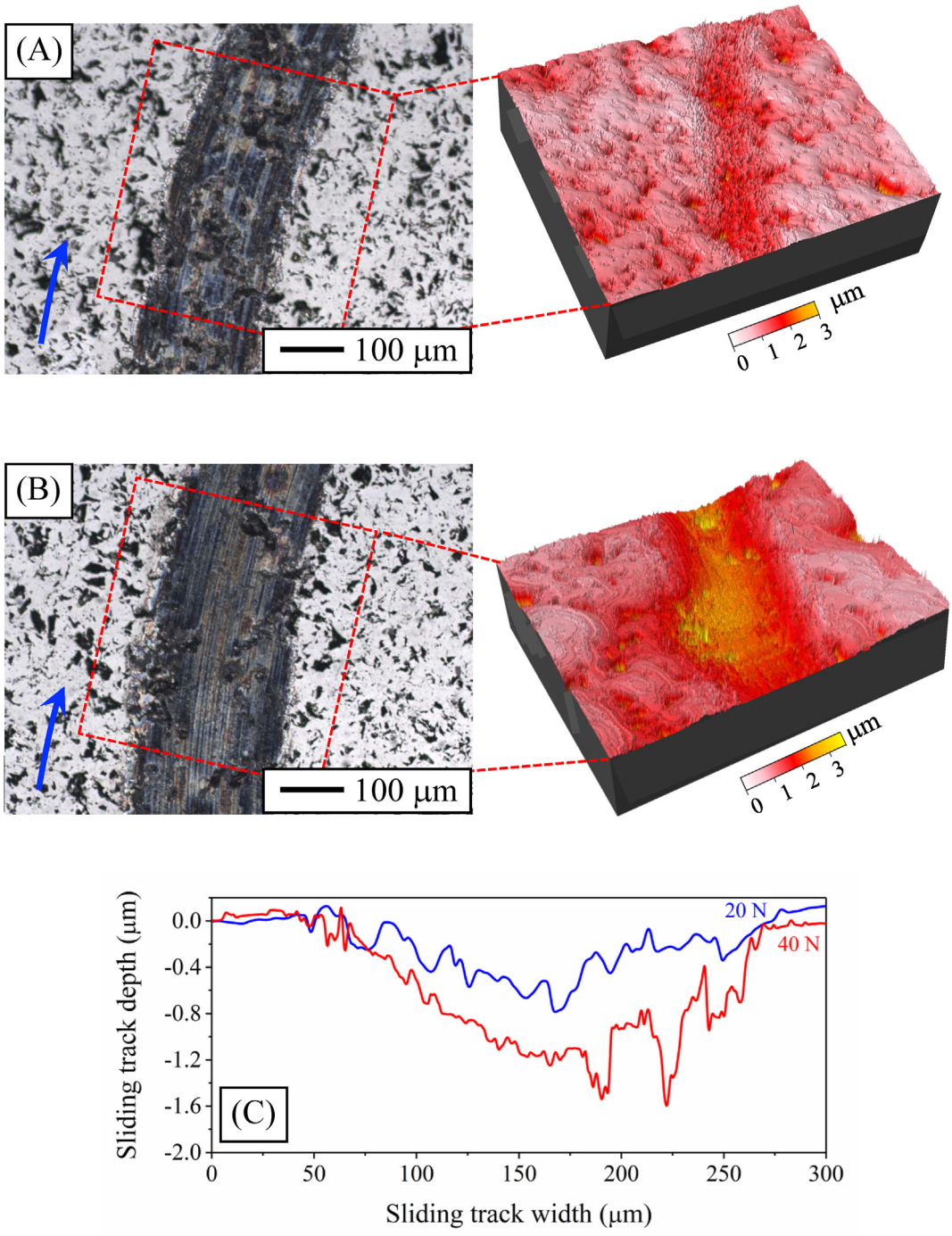

Fig. 15 – Bright-field OM images of the residual sliding tracks generated in the ZrB_2–hardened Zr_3Al_2 intermetallic–ceramic composite during the tests at loads of (A) 20 and (B) 40 N, as well as 3-D OP images of them (as marked in the OM images). (C) Typical 2-D OP profiles of the residual sliding tracks, as extracted from corresponding 3-D OP images. Pitted zones in (A)–(B) are not pores, but micro-chips generated during the grinding and polishing stages. The arrows denote the sliding direction.

sliding wear as being very mild [11,12]. This is entirely consistent with the expectation derived from the low friction (Fig. 14). Interestingly, the SSWRs are slightly higher than the SFWRs despite the damage being distributed over a much larger area, attributable to (i) delayed removal of the contact asperities, which are also more abundant, and (ii) delayed formation of the protective oxide tribolayers.

As mentioned above, the low CoFs in Fig. 14 indirectly suggest the formation of self-lubricating oxide tribolayers also during the sliding tests, something that the OM images of the sliding tracks in Fig. 15 apparently corroborate. Nonetheless, for direct evidence of this, Fig. 16 shows the SEM images of the sliding tracks produced at 20 N (Figs. 16A) and 40 N (Fig. 16B) loads, together with the corresponding elemental composition

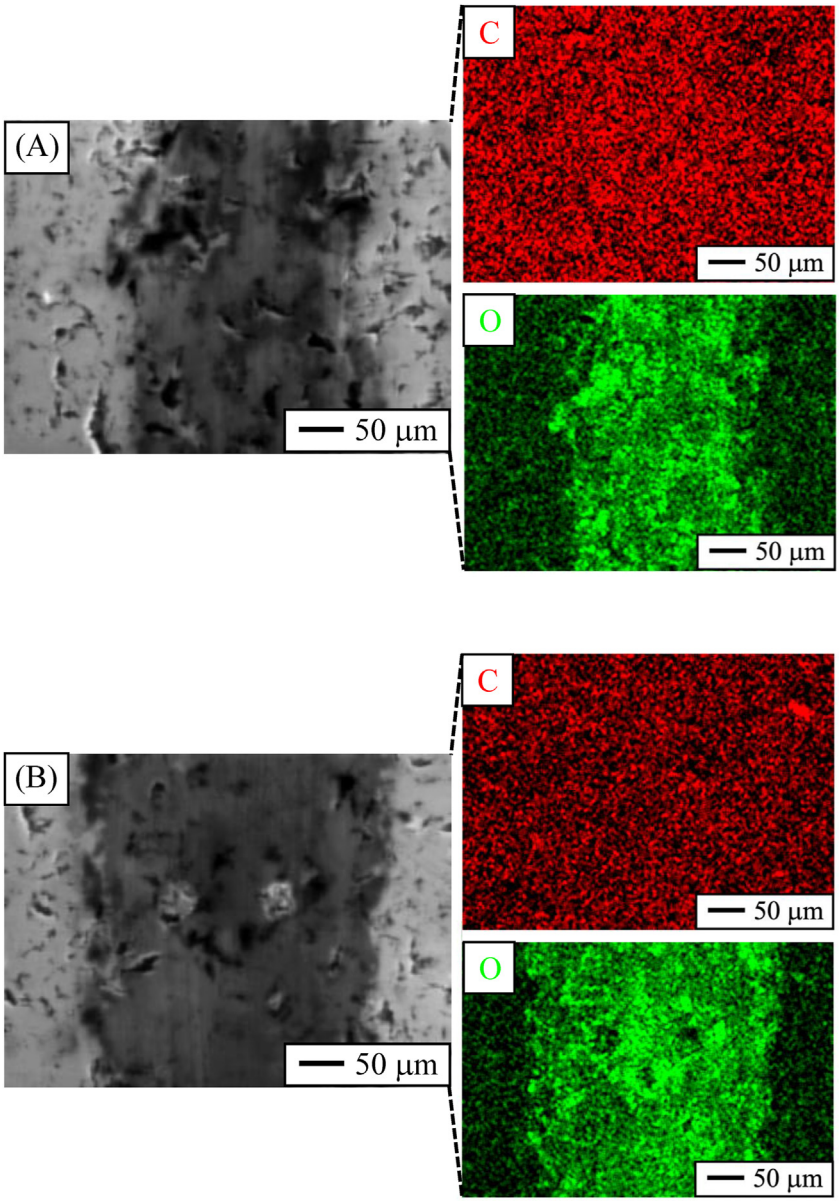

Fig. 16 – SEM images and the corresponding elemental composition maps of C and O acquired by EDS of the residual sliding tracks generated in the ZrB_2–hardened Zr_3Al_2 intermetallic–ceramic composite during the tests at loads of (A) 20 and (B) 40 N. Pitted zones are not pores, but micro-chips generated during the grinding and polishing stages.

maps of C and O acquired by EDS. It is clearly evident from these composition maps that oxide tribolayers formed in the worn zone, again attributable to the surface oxidation of the contact zone as a consequence of the frictional heating generated during the sliding tests in air atmosphere. Again, examination of the counter-balls by OM revealed no damage compatible with material transfer, thus corroborating that the tribolayers are not carbon. Therefore, this demonstrates the occurrence of mild oxidative sliding wear. Again however, the oxide tribolayers also covered the sliding tracks well, thus protecting and self-lubricating the sliding contact.

Fig. 17 shows SEM images of the sliding damage generated at 20 and 40 N loads. It can be seen in the two cases that underneath the thin oxide tribolayers (because they are relatively "transparent" to the electron beam), again oxides of both Zr_3Al_2 and ZrB_2 because the Zr_3Al_2 and ZrB_2 rich regions in the bi-phasic microstructure of this composite have micrometre sizes, there are shallow scratches, typical of plastic grooves, parallel to the sliding direction, as well as limited fracture-induced material removal mostly at pre-existing chips. All this evinces just slight abrasion of the surface with generation of little wear debris, and is therefore indicative of the occurrence of mild mechanical sliding wear.

Taken together, these observations and results indicate that the present Zr_3Al_2–ZrB_2 composite is also resistant to sliding wear – *i.e.*, resistance of the order of 10^7 $(N \cdot m)/mm^3$ – and is therefore a potential candidate for the fabrication of components subjected to relative movements (which nonetheless

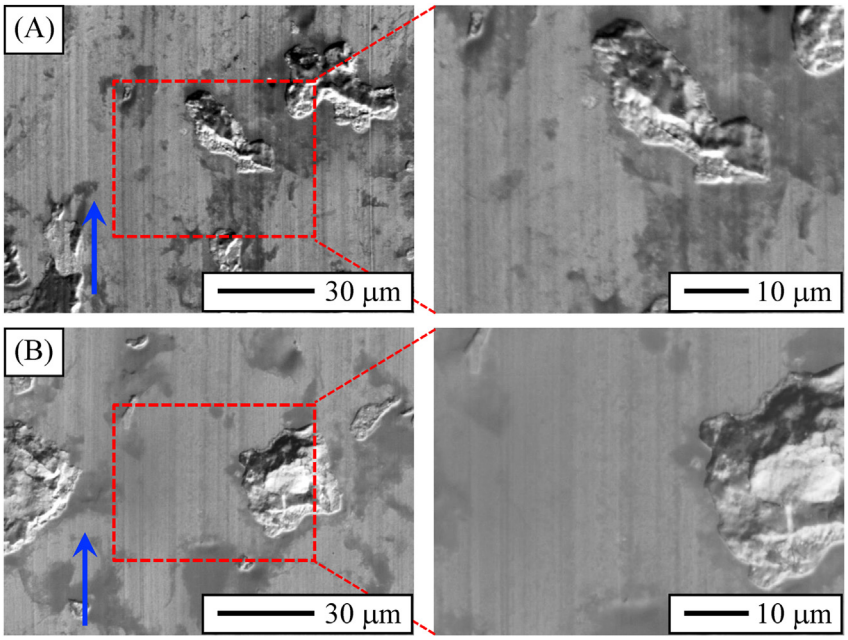

Fig. 17 – SEM images of the damage inside the residual sliding tracks generated in the ZrB_2–hardened Zr_3Al_2 intermetallic–ceramic composite during the tests at loads of (A) 20 and (B) 40 N. Note that these SEM images were intentionally taken at zones where the oxide tribolayers had partially failed, but that lower-magnification SEM images demonstrated that the extent of this phenomenon is limited.

also requires study and validation for each particular tribosystem). In this first study against ultrahard diamond, the Zr_3Al_2–ZrB_2 composite wore initially by mild mechanical sliding wear, undergoing slight two-body abrasion and to a lesser extent three-body abrasion, until an oxide tribolayer eventually formed dictating the onset of mild oxidative sliding wear. The severities of both the mechanical abrasion and the oxidative wear increased with increasing applied load, but with the former dominating over the latter to give hollow-type sliding tracks. In any case, as was already the case for fretting wear, once formed the oxide tribolayers were also "protective" in the case of sliding wear and avoided much more severe mechanical abrasion during the remainder of the sliding tests.

4. Conclusions

A model tribological study was conducted on the unlubricated scratch, fretting, and sliding wear of a very recently developed ZrB_2–hardened Zr_3Al_2 intermetallic–ceramic composite, using diamond as counterpart. Based on the experimental results and analyses, the following conclusion can be drawn:

1. Under scratch wear, the Zr_3Al_2–ZrB_2 composite undergoes a ductile-to-brittle transition with increasing applied load, exhibiting increasing plastic damage from low loads and eventually at higher loads also additional macro-chipping and even massive meso-/macro-chipping.
2. The Zr_3Al_2–ZrB_2 composite is resistant to fretting wear, exhibiting low SFWRs and mild damage caused first by fretting fatigue and then by fretting oxidation, both of increasing severity with increasing applied load. Fretting fatigue dominates at low and intermediate loads, and fretting oxidation does so at high loads. Subjected to fretting wear, the Zr_3Al_2–ZrB_2 composite eventually develops protective, self-lubricating oxide tribolayers.
3. The Zr_3Al_2–ZrB_2 composite is resistant to sliding wear, exhibiting low SSWRs and mild damage caused first by mechanical sliding wear and then by oxidative sliding wear, both of increasing severity with increasing applied load but with the former dominating over the latter. Subjected to sliding wear, the Zr_3Al_2–ZrB_2 composite also eventually develops protective, self-lubricating oxide tribolayers.
4. These Zr_3Al_2–ZrB_2 composites seem promising candidate materials for tribological applications, and therefore deserve further investigation under an ample set of possible engineeringly-relevant wear conditions.

Declaration of Competing Interest

The authors declare that they have no known competing financial interests or personal relationships that could have appeared to influence the work reported in this paper.

Acknowledgements

The authors acknowledge the financial support provided by the Spanish Ministry of Science and Innovation under Grant no. PID2019-103847RJ-I00, Junta de Andalucía under Grant no. P18-RTJ-1972, and Junta de Extremadura under Grants nos. IB20017 and GR21170 (co-financed with FEDER funds).

REFERENCES

[1] Duan YH, Huang B, Sun Y, Peng MJ, Zhou SG. Stability, elastic properties and electronic structures of the stable Zr–Al intermetallic compounds: a first-principles investigation. J Alloys Compd 2014;590:50–60.

[2] Laik A, Bhanumurthy K, Kale GB. Intermetallics in the Zr–Al diffusion zone. Intermetallics 2004;12(1):69–74.

[3] Schulson EM. In: Westbrook JH, Fleischer RL, editors. Intermetallic compounds, vol. 2. New York: John Wiley & Sons; 1994.

[4] He W, Chen X, Liu N, Luan B, Yuan G, Liu Q. Cryo-rolling enhanced inhomogeneous deformation and recrystallization grain growth of a zirconium alloy. J Alloys Compd 2017;699:160–9.

[5] Zhang X, Zhang B, Liu SG, Xia CQ, Zhang XY, Ma MZ, et al. Microstructures and mechanical properties of Zr–Al binary alloys processed by hot-rolling. Mater Sci Eng 2020;773:138723.

[6] Kutty TRG, Ravi K, Ganguly C. Studies on hot hardness of Zr and its alloys for nuclear reactors. J Nucl Mater 1999;265(1):91–9.

[7] Kondo R, Nomura N, Suyalatu, Tsutsumi Y, Doi H, Hanawa T. Microstructure and mechanical properties of as-cast Zr–Nb alloys. Acta Biomater 2011;7(12):4278–84.

[8] Russell RB. Coefficients of thermal expansion for zirconium. JOM 1954;6(9):1045–52.

[9] Murray J, Peruzzi A, Abriata JP. The Al–Zr (aluminum–zirconium) system. J Phase Equil 1992;13(2):277–91.

[10] López-Arenal J, Moshtaghioun BM, Cumbrera FL, Gómez-García D, Ortiz AL. Powder-metallurgy fabrication of ZrB_2–hardened Zr_3Al_2 intermetallic composites by high-energy ball-milling and reactive spark-plasma sintering. J Mater Res Technol 2022;21:617–26.

[11] Bhushan B. Modern tribology handbook. Boca Raton, USA: CRC Press; 2001.

[12] Stachowiak GW, Batchelor AW. Engineering tribology. 3rd ed. Oxford, UK: Elsevier Butterworth-Heinemann; 2005.

[13] Stachowiak GW, Batchelor AW, Stachowiak GB. Experimental methods in tribology. 1st ed. Oxford, UK: Elsevier Butterworth-Heinemann; 2004.

[14] Lawn BR, Padture NP, Braun LM, Bennison SJ. Model for toughness curves in two-phase ceramics: I, basic fracture mechanics. J Am Ceram Soc 1993;76(9):2235–40.

[15] Padture NP, Runyan JL, Bennison SJ, Braun LM, Lawn BR. Model for toughness curves in two-phase ceramics: II, microstructural variables. J Am Ceram Soc 1993;76(9):2241–7.

[16] Lawn BR. Chipping: a pervasive presence in nature, science and technology. J. Mat. Sci. 2021;56:8396–405.

[17] Huang H, Li X, Mu D, Lawn BR. Science and art of ductile grinding of brittle solids. Int J Mach Tool Manufact 2021;161:103675.

[18] Lawn BR, Huang H, Lu M, Borrero-López O, Zhang Y. Threshold damage mechanisms in brittle solids and their impact on advanced technologies. Acta Mater 2022;232:117921.

[19] Lawn BR, Borrero-López O, Huang H, Zhang Y. Micromechanics of machining and wear in hard and brittle materials. J Am Ceram Soc 2021;104(1):5–22.

[20] Neu RW. Progress in standardization of fretting fatigue terminology and testing. Tribol Int 2011;44:1371–7.